



HAL
open science

ALMA-ALPINE [CII] survey: The sub-kpc morphology of three main sequence galaxy systems at $z \sim 4.5$ revealed by ALMA

T. Devereaux, P. Cassata, E. Ibar, C. Accard, C. Guillaume, M. Béthermin, M. Dessauges-Zavadsky, A. Faisst, G. C. Jones, A. Zanella, et al.

► To cite this version:

T. Devereaux, P. Cassata, E. Ibar, C. Accard, C. Guillaume, et al.. ALMA-ALPINE [CII] survey: The sub-kpc morphology of three main sequence galaxy systems at $z \sim 4.5$ revealed by ALMA. *Astronomy and Astrophysics - A&A*, 2024, 686, 10.1051/0004-6361/202348511 . insu-04643181

HAL Id: insu-04643181

<https://insu.hal.science/insu-04643181v1>

Submitted on 10 Jul 2024



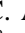











HAL is a multi-disciplinary open access archive for the deposit and dissemination of scientific research documents, whether they are published or not. The documents may come from teaching and research institutions in France or abroad, or from public or private research centers.

L'archive ouverte pluridisciplinaire **HAL**, est destinée au dépôt et à la diffusion de documents scientifiques de niveau recherche, publiés ou non, émanant des établissements d'enseignement et de recherche français ou étrangers, des laboratoires publics ou privés.



Distributed under a Creative Commons Attribution 4.0 International License

ALMA-ALPINE [CII] survey: The sub-kpc morphology of three main sequence galaxy systems at $z \sim 4.5$ revealed by ALMA[★]

T. Devereaux¹, P. Cassata^{1,2}, E. Ibar³ , C. Accard⁴ , C. Guillaume⁴ , M. Béthermin^{4,5} ,
M. Dessauges-Zavadsky⁶ , A. Faisst⁷, G. C. Jones⁸, A. Zanella², S. Bardelli⁹ , M. Boquien¹⁰, E. D’Onghia¹¹,
M. Giavalisco¹² , M. Ginolfi^{13,14}, R. Gobat¹⁵, C. C. Hayward¹⁶ , A. M. Koekemoer¹⁷ , B. Lemaux^{18,19},
G. Magdis^{20,21,22} , H. Mendez-Hernandez^{23,24}, J. Molina²⁵, F. Pozzi^{26,9}, M. Romano^{27,2} , L. Tasca⁵, D. Vergani⁹ ,
G. Zamorani⁹ , and E. Zucca⁹ 

(Affiliations can be found after the references)

Received 6 November 2023 / Accepted 4 March 2024

ABSTRACT

Context. Going from a redshift of 6 down to nearly 4, galaxies grow rapidly from low-mass galaxies towards the more mature types of massive galaxies seen at cosmic noon. Growth via gas accretion and mergers undoubtedly shape this evolution, however, there is considerable uncertainty at present over the contribution of each of these processes to the overall evolution of galaxies. Furthermore, previous characterisations of the morphology of galaxies in the molecular gas phase have been limited by the coarse resolution of earlier observations.

Aims. In this work, we utilise new high-resolution ALMA [CII] observations to analyse three main sequence (MS) galaxy systems at a redshift of $z \sim 4.5$ and at resolutions of up to $0.15''$. This approach enables us to investigate the morphology and kinematics on a kpc scale and understand the processes at play as well as the classifications of galaxies at high resolution. Thanks to this unique window, we are able to gain insights into the molecular gas of MS galaxies undergoing mass assembly in the early Universe.

Methods. We used intensity and velocity maps, position-velocity diagrams, and radial profiles of [CII] in combination with dust continuum maps to analyse the morphology and kinematics of the three systems.

Results. In general, we find that the high-resolution ALMA data reveal more complex morpho-kinematic properties. For one galaxy in our sample, we identified interaction-induced clumps, demonstrating the profound effect that mergers have on the molecular gas in galaxies, which is consistent with what has been suggested by recent simulations. One galaxy that was previously classified as dispersion-dominated turned out to show two bright [CII] emission regions, which could either be classified as merging galaxies or massive star-forming regions within the galaxy itself. The high-resolution data for the other dispersion dominated object also revealed clumps of [CII] that had not been identified previously. Within the sample, we might also detect star-formation powered outflows (or outflows from active galactic nuclei) that appear to be fuelling diffuse gas regions and enriching the circumgalactic medium. The new high-resolution ALMA data we present in this paper reveal that the galaxies in our sample are much more complex than they previously appeared in the low-resolution ALPINE data. In particular, we find evidence of merger induced clumps in the galaxy DC8187, along with signs of merging components for the other two objects. This may be evidence that the number of mergers at high redshift are significantly underestimated at present.

Key words. galaxies: evolution – galaxies: formation – galaxies: high-redshift – galaxies: ISM – galaxies: star formation – submillimeter: galaxies

1. Introduction

The epoch between $z \sim 6$ and $z \sim 2$ is crucial for understanding galaxy evolution: during these ~ 2 Gyr of cosmic time the star formation rate density of the Universe (SFRD) increases by a factor of 20 (Madau & Dickinson 2014), with the average specific star-formation rate of individual galaxies going up by about the same amount (Tasca et al. 2015; Schreiber et al. 2015; Tomczak et al. 2016); over the same time span, galaxies evolve from small, metal-poor, dust-free, and turbulent objects in the very early Universe (Maiolino et al. 2024; Finkelstein et al. 2022) to more regular morphologies at $z \sim 2$ (van der Wel et al. 2014; Zhang et al. 2019), with ordered disks (Förster Schreiber et al. 2009) and significant dust and metal content (Troncoso et al. 2014; Popping et al. 2023).

While it is thought that galaxies at these epochs grow via mergers and the accretion of gas from galactic halos, the relative importance of the two mechanisms is not clear.

[★] The reduced datacubes are available at the CDS via anonymous ftp to cdsarc.cds.unistra.fr (130.79.128.5) or via <https://cdsarc.cds.unistra.fr/viz-bin/cat/J/A+A/686/A156>

Förster Schreiber & Wuyts (2020) suggested that gas accretion dominates, while (Romano et al. 2021) in addition to simulations (i.e. Vallini et al. 2013; Kohandel et al. 2019; Pallottini et al. 2022) suggest a potential build-up from a combination of major mergers, minor mergers, and gas accretion. To make significant progress, it is vital to unveil the morphokinematic properties of galaxies $4 < z < 6$, when these mechanisms are working at full strength. At the same time, it is essential to revealing the interplay between the stars, dust, and molecular gas that constitute the fuel from which stars can form.

While a combination of ground based telescopes, such as the Visible and Infrared Survey Telescope for Astronomy (VISTA) with space observatories such as *Hubble* Space Telescope (HST), *Spitzer*, and *James Webb* Space Telescope (JWST) offers the capability to probe stellar component of galaxies up to $z \sim 6$ and beyond (Song et al. 2016; Naidu et al. 2022; Harikane et al. 2023), observing molecular gas at redshifts beyond the peak epoch of cosmic star formation remains challenging. H_2 cannot be observed directly, so studies have used tracers such as CO (see review by Bolatto et al. 2013) and [CI] (e.g. Walter et al. 2011). However, the low-excitation transitions of the CO molecule

((1–0) and (2–1)), which can better probe the molecular gas content of galaxies, are inaccessible to the Atacama Large Molecular Array (ALMA) beyond $z \sim 3$ Carilli & Walter (2013); in addition, they are too faint to be detected with reasonable integration times with Very Large Array (VLA; D’Eugenio et al. 2023). In recent years, this has led to the use of [CII] $\lambda 158 \mu\text{m}$ transition as a tracer for the molecular gas at high redshifts. The [CII] emission line is one of the brightest lines in the spectra of galaxies at high redshifts – owing to its ability to trace the ionised, molecular, and neutral phases. Whilst [CII] has typically been used as a star formation tracer (e.g. De Looze et al. 2014), more recent works suggest that the majority of the [CII] flux in galaxies comes from molecular clouds. Calibrations of the [CII] line as a molecular gas tracer in high-redshift galaxies have been studied in Zanella et al. (2018). In Vizgan et al. (2022), it was eventually confirmed that the [CII] luminosity is more tightly related to $-M(\text{H}_2)$, with the correlation between [CII] and SFR arising from the Kennicutt–Schmidt relation (Kennicutt 1998).

The ALMA Large Program to INvestigate [CII] at Early times (ALPINE) survey (Le Fèvre et al. 2020; Béthermin et al. 2020; Faisst et al. 2020) was designed to directly explore the interplay between stars, dust, and molecular gas mass in normal main sequence (MS) galaxies at $4.5 < z < 6$ – the redshift range where galaxies transition from lower mass primordial galaxies to more evolved galaxies at cosmic noon. There, [CII] was used as a tracer for molecular gas to reveal the molecular gas content of galaxies (Dessauges-Zavadsky et al. 2020): using the calibration provided in Zanella et al. (2018), the authors found a good agreement between [CII] luminosity, the dust mass (extrapolated from the continuum flux) and dynamical masses, supporting [CII] as a reliable tracer of molecular gas (Le Fèvre et al. 2020; Romano et al. 2021; see also Jones et al. 2021) found that 40% of galaxies in the sample of 118 galaxies are mergers, 20% were found to be characterised by a high-velocity dispersion and extended components and 11% of galaxies were found to be rotating disks.

Among the ALPINE galaxies that are resolved, a large number appear to have an underlying gas halo (Fujimoto et al. 2020). Recent semi-analytical models indicate these halos can be produced by star-formation driven outflows (Pizzati et al. 2022). Due to the limited ($\sim 1''$) resolution of ALPINE, the majority of galaxies were poorly resolved, meaning diffuse gas could not be distinguished from compact regions. Furthermore, the low resolution severely impacted the ability of ALPINE to trace the properties (i.e. mergers, clumps, and components in the velocity) in (some of) these galaxies.

Simons et al. (2019) showed that at low resolution, close mergers can be indistinguishable from disks. This is an issue seen in the majority of galaxies observed in [CII] thus far. The low resolution ($\sim 0.7''$) of the ALMA observations for the ALPINE survey has limited the number of systems of multiple galaxies which can be spatially resolved from one another and may thus be identified as mergers. One of the best examples of a merger in [CII] is extensively studied in Jones et al. (2020). The authors used ALPINE data to show a massive system undergoing mass assembly via the merger of three galaxies. This example possibly presents the most idealised case of a major merger in which three merging galaxies can be clearly resolved from each other spatially as well as in terms of velocity.

When resolved at kpc and sub-kpc scales, galaxies can appear clumpy in star formation tracers (e.g. Claeysens et al. 2023). Therefore, the coarse resolution of ALPINE, which allows for a resolution on scales from ~ 5 – 8 kpc, is not sufficient to resolve these clumps spatially. The dominant theory is

that clumpiness comes from gravitational instability (Dekel et al. 2009) or via mergers and interactions (Di Matteo et al. 2008). At this redshift and with the resolution of current observations, it has been suggested what we are observing is primarily mergers Zanella et al. (2021). The lack of high-resolution spectroscopic data sets has significantly hindered our ability to uncover the kinematics in these galaxies and impeded detections of the imprints of mergers upon galaxies and how they evolve.

There exist only a small number of spatially resolved observations targeting molecular gas, in the high redshift ($z > 4$) regime; for example (Neeleman et al. 2023; Shao et al. 2022; Roman-Oliveira et al. 2023). Roman-Oliveira et al. (2023) studied four starburst galaxies, finding the majority of them to be rotating disks. Observations of merging systems (Oteo et al. 2018; Litke et al. 2019) identified irregular components of gas emission. However, these surveys all traced star-bursting galaxies with SFRs $> 1000 M_{\odot} \text{yr}^{-1}$, providing insights into only a subdominant population of galaxies at this redshift. Herrera-Camus et al. (2021) traced a $z \sim 5.5$ typical star forming galaxy at $0.3''$ angular resolution finding evidence of star formation outflows and extended emission, as well as rotation. The authors also found evidence of an extended molecular gas halo surrounding the galaxy. The small number of spatially resolved galaxies at this redshift leaves much uncertainty for the processes occurring in these galaxies – particularly for MS mergers and dispersion-dominated galaxies (which were found to be the majority from ALPINE).

In this paper, we use brand new high-resolution ALMA [CII] observations to analyse three MS galaxy systems at resolutions of up to $0.15''$ and investigate the morphology and kinematics on a kpc scale. We also aim to understand the processes at play and the classifications of galaxies at high resolution, offering useful insights into the molecular gas of MS galaxies undergoing mass assembly. This paper assumes a Λ -CDM cosmology, with $h_0 = 0.7$, $\Omega_{\Lambda} = 0.7$, and $\Omega_{\text{m}} = 0.3$. A Chabrier initial mass function (IMF) is also assumed (Chabrier 2003).

2. The sample

This paper focuses on three galaxies at redshifts ~ 4.5 that were studied in Jones et al. (2021). All were found to be on the MS at this redshift (Faisst et al. 2020). The criteria for selecting these galaxies for a high-resolution follow-up were as follows: (i) [CII] peak flux densities higher than 10 mJy beam^{-1} to ensure dynamical studies in reasonable integration times; (ii) a strongly detected continuum ($> 7\sigma$); (iii) the [CII] and continuum appear aligned in ALPINE observation, and, finally, (iv) the HST images of these galaxies showed no evidence of late stage mergers. In this section, we present the properties of these galaxies, as obtained from the analysis of the low-resolution ALPINE data.

2.1. DC8737

DEIMOS_COSMOS_873756 (hereafter, DC8737) is the brightest galaxy in the ALPINE survey, at a spectroscopic redshift of $z = 4.5480$. At the coarse ~ 0.7 resolution of the original ALPINE data, it shows no signs of rotation; it does show a high-velocity dispersion. The [CII] emission is extended to the east. The galaxy was classified as dispersion dominated because the main component dominates the field and the [CII] line is very broad, with a FWHM of 526 km s^{-1} (Jones et al. 2021; Le Fèvre et al. 2020). In Cassata et al. (2020), this galaxy is found to be a Ly α emitter in the central region.

2.2. VC8326

VUDS_COSMOS_5101218326 (hereafter, VC8326) has a redshift of $z = 4.5678$. Jones et al. (2021) modelled its velocity map with 3D-Based Analysis of Rotating Object via Line Observations (3D-BAROLO; Di Teodoro & Fraternali 2015), finding that this object is likely to be an extended dispersion-dominated galaxy. HST/ACS *F814W* imaging (Koekemoer et al. 2007) from the COSMOS survey, targeting the rest-frame UV, reveal extended emission over $1''$ scales. VC8326 is in the central regions of the most massive component of the PCI J1001+0220 protocluster (Lemaux et al. 2018; Staab et al. 2024).

2.3. DC8187

DEIMOS_COSMOS_818760 (hereafter, DC 8187) consists of three galaxies at $z = 4.56038$, $z = 4.56628$, and $z = 4.56229$, extensively studied in Jones et al. (2020). The eastern and central sources are the two largest and brightest and are found to be close both spatially and in velocity. Therefore, they are considered to be undergoing a major merger. A third source (separate in velocity by $\sim 300 \text{ km s}^{-1}$ and spatially by 18 kpc) is detected nearby. It is likely going to merge with the main system in the future. The velocity map of this galaxy showed signs of rotation or tidal disruption and it was found in Jones et al. (2020) to have the lowest [CII] luminosity of the three sources.

3. Data processing and analysis

3.1. Observations and data reduction

The data used in this paper were obtained between 2020 and 2021 as part of the ALMA project 2019.1.00226.S (P.I.: E. Ibar). Configurations C43-5 and C43-3 were used, producing resolutions of $0.15''$ (high resolution, HR) and $0.3''$ (medium resolution, MR), respectively. Objects were observed for 937 s and 1975 s in C43-5 and C43-3, respectively, for each object (which corresponds to only a fraction of the 30 h originally planned for the observations). The spectral setup was such that all three galaxies were able to be observed within a loop with exactly the same spectral setup, using the same phase calibrator; this was to reduce the overheads and maximise the total integration times. Additionally, we also included in the analysis the lower resolution (LR) data, available from ALPINE (2017.1.00428.L, P.I.: Le Fèvre).

The high-resolution, medium-resolution, and low-resolution data were processed, independently for each observation, using the standard ALMA pipeline to produce calibrated uv datasets for each observation and for each source. The pipeline calibration was manually checked and no issues were found with the calibration. Channels containing line emission were identified and excluded, a buffer of 10 km s^{-1} either side of the emission was ensured to prevent any contamination from the wings of the line emission. The continuum was then subtracted using the CASA task `uvcontsub` to produce the continuum subtracted visibility file for each resolution.

Due to the nature of interferometry, high-resolution images typically fail to pick up extended emission. In the case of these observations, the maximum recoverable scale is larger than the size of the galaxies and thus diffuse emission can be detected by these high-resolution observations (if they have sufficient exposure time). However, with ALMA, high-resolution observations are noisier than low-resolution observations. This means high-resolution observations fail to pick up fainter, diffuse emission

Table 1. RMS of each [CII] intensity map (moment 0) in $\text{Jy km s}^{-1} \text{ beam}^{-1}$.

Galaxy	HR+MR	HR+MR+LR
VC8326	64	70
DC8737	76	59
DC8187	78	67

Table 2. Beam size of each resolution concatenation in arc seconds.

Galaxy	HR+MR beam	HR+MR+LR beam
VC8326	0.232×0.158	0.313×0.242
DC8737	0.224×0.154	0.349×0.273
DC8187	0.241×0.179	0.294×0.231

Notes. These are the best-fit 2D Gaussian FWHMs of the synthesised beam.

without long integration times – which are unrealistic in the case of a competitive interferometer such as ALMA. However, it is possible to concatenate low-resolution data with higher resolution data to build up a picture of both the compact and extended emission. Therefore, a combination of visibility files is used in this paper. First, a concatenation of the high and medium resolution was made using `concat` for each source. It was decided to combine the highest resolutions observations ($0.15''$ and $0.3''$) to a single concatenation in order to maximise the S/N. Secondly, a high+medium+low resolution concatenation was made using the CASA task `concat` for each source. This concatenation allows for a better coverage of the uv -plane, allowing the tracing of both extended and compact components of emission. From here on out, we refer to these concatenations as HR+MR+LR for all three resolutions combined and HR+MR – for the high and medium resolution concatenation.

To produce the final data cubes, cleaning was undertaken using the CASA task `tclean`, a Briggs weighting (with `robust=0.5`) was chosen to best compromise between resolution and sensitivity. A dirty image was produced and the RMS per pixel (of the peak channel) estimated using an aperture located outside of the galaxy (to avoid emission from the galaxy). All galaxies were cleaned to a threshold of $2.5 \times \text{RMS}$. The resultant RMS per pixel and synthesised beam for each moment 0 map are shown in Tables 1 and 2.

3.2. Production of moment 0 and 1 maps

For each source, at each resolution, moment 0 and moment 1 maps were produced for channels that contain line emission. The moment 0 map shows the spatial distribution of line emission, whereas the moment 1 map shows the velocity distribution of line emission. The optimum velocity range of the 1D spectra which maximises the S/N of the line emission was found using the procedure used in Zanella et al. (2018), this is described as follows. The total signal-to-noise ratio (S/N) was measured within an aperture of diameter $3''$ (for the HR+MR+LR resolution concatenation) or $1.5''$ for the HR+MR cubes. This was calculated for all possible channel ranges in the data-cube, noting the velocity range that maximised the S/N is considered to be the channel range containing the line emission.

Moment 0 and 1 maps were produced using the CASA task `immoments` using the channels previously selected to contain

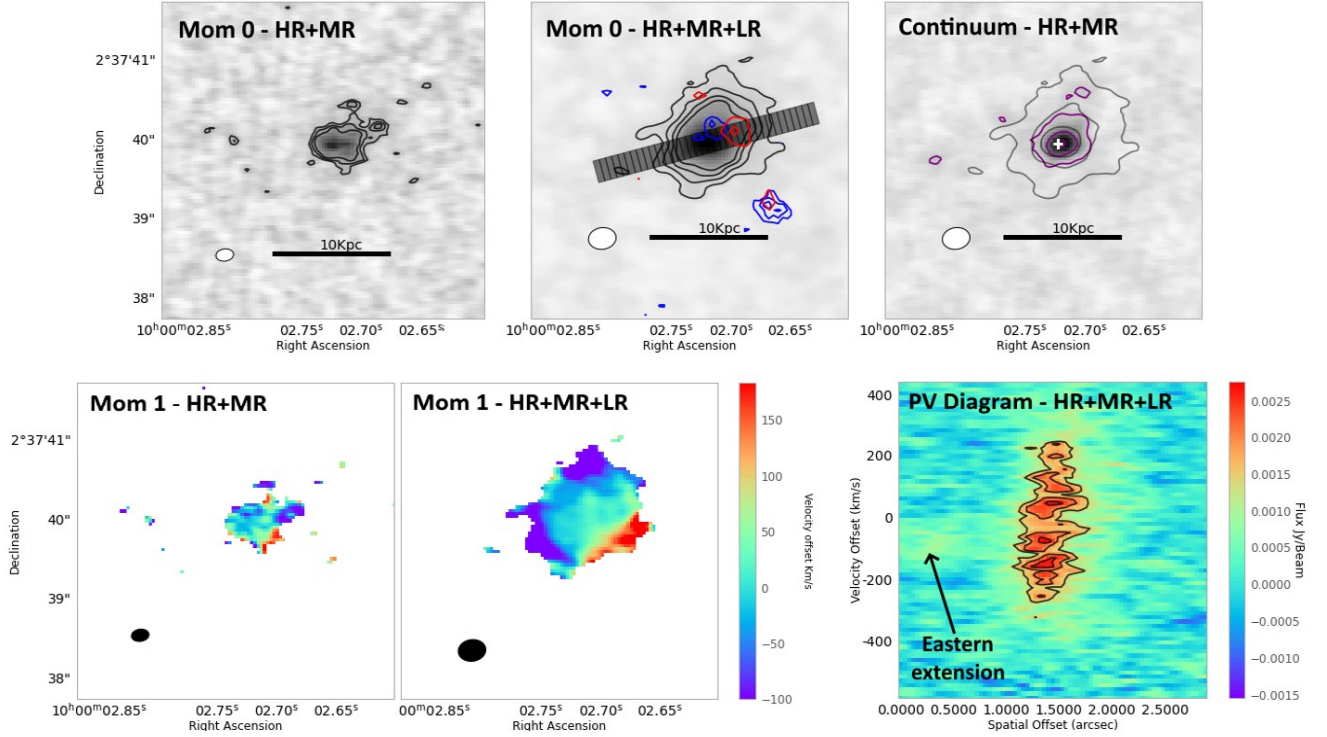


Fig. 1. Summary of maps produced for DC8737. Top line shows the moment 0 maps, from left to right: HR+MR (with S/N contours from $\pm 5, 6, 7, \dots \sigma$) and HR+MR+LR with S/N contours of $\pm 5, 6, 7, \dots \sigma$, along with HST/ACS *F814W* (Koekemoer et al. 2007; blue; 3, 5, 7, 9 σ) and *K*-band (red; 3, 4 σ) continuum map (with continuum and [CII] contours from 5 σ in purple and black, respectively). The second line shows the moment 1 maps cut to 5 σ , for the HR+MR and the HR+MR+LR configurations and the PV diagram taken in the HR+MR+LR concatenation – using the slit shown on the top line – with contours of 0.7, 0.8, and 0.9x the peak value.

line emission. For the HR+MR and HR+MR+LR moment 1 maps, a σ -cut was made (between 3–5 σ depending on the galaxies morphology); that is, any pixel with a S/N less than defined above was set to null. This ensures the velocity map is only showing pixels likely to be a constituent of the galaxy.

Continuum maps were produced for each source. These were produced directly from non-continuum subtracted visibility files. The same concatenations as described in Sect. 3.1 were created. All spectral windows in the band were selected, however the channels found to contain line emission (as described above) were excluded. Using tclean, with a mfs mode and a Briggs weighting (robust=0.5), a dirty continuum image was produced for each observation. Using an aperture of an empty background region, the RMS was estimated and cleaning was repeated to $2.5 \times \text{RMS}$ in order to produce clean continuum maps.

The moment 0 maps and moment 1 maps are shown in Figs. 1–3. For the HR+MR+LR maps, which give the best view of the compact + extended emission, *K*-band, VISTA observations (matching the rest-frame optical), and HST observations (matching the rest-frame ultraviolet) are contoured to compare the stellar distribution and obscured star formation to the [CII] distribution. The continuum maps are also shown in the same figures, along with [CII] contours to compare the obscured star formation (from continuum) and gas distributions (shown by the [CII]).

3.3. Fidelity of galaxy components

The moment 0 maps show that the high-resolution observations reveal complex components (i.e. clumps, compact regions) that were previously not observable due to the coarse resolution of

the ALPINE survey. However, there is a risk that spurious emission from noise can be misidentified as emission from the galaxy. Therefore, to ensure any detections are significant, we adopted the method from Walter et al. (2016); thus, we assumed that the noise is Gaussian and the number of positive and negative peaks above a given flux limit should be the same, if no detection is present. Real and robust detections should instead only appear as positive peaks. Using Eq. (1), we estimate the term coined in Walter et al. (2016), namely, the “fidelity” as:

$$\text{Fidelity}(S/N) = 1 - \frac{N_{\text{neg}}(S/N)}{N_{\text{pos}}(S/N)}. \quad (1)$$

In practice, the fidelity compares the ratio of non physical negative noise peaks to potentially real positive peaks for a given S/N. The S/N where this fidelity is equal to 60% is the value that is considered the minimum for a detection to be considered real for a given number of connected pixels. In order to estimate the fidelity of individual components, we count the number of positive sources of comparable or larger number of connected pixels as the component at a given S/N and the same is conducted for negative sources; the comparison of the two, according to Eq. (1), gives the fidelity of such component.

3.4. [CII] flux analysis

Performing the photometry of the [CII] and continuum emission in these galaxies is a non-trivial task. DC8737, DC8187, and VC8326 have clumpy or irregular morphologies which are poorly fit by a two-dimensional (2D) Gaussian. Therefore, aperture photometry was conducted on the moment 0 maps, with aperture sizes that must be carefully selected as not to miss

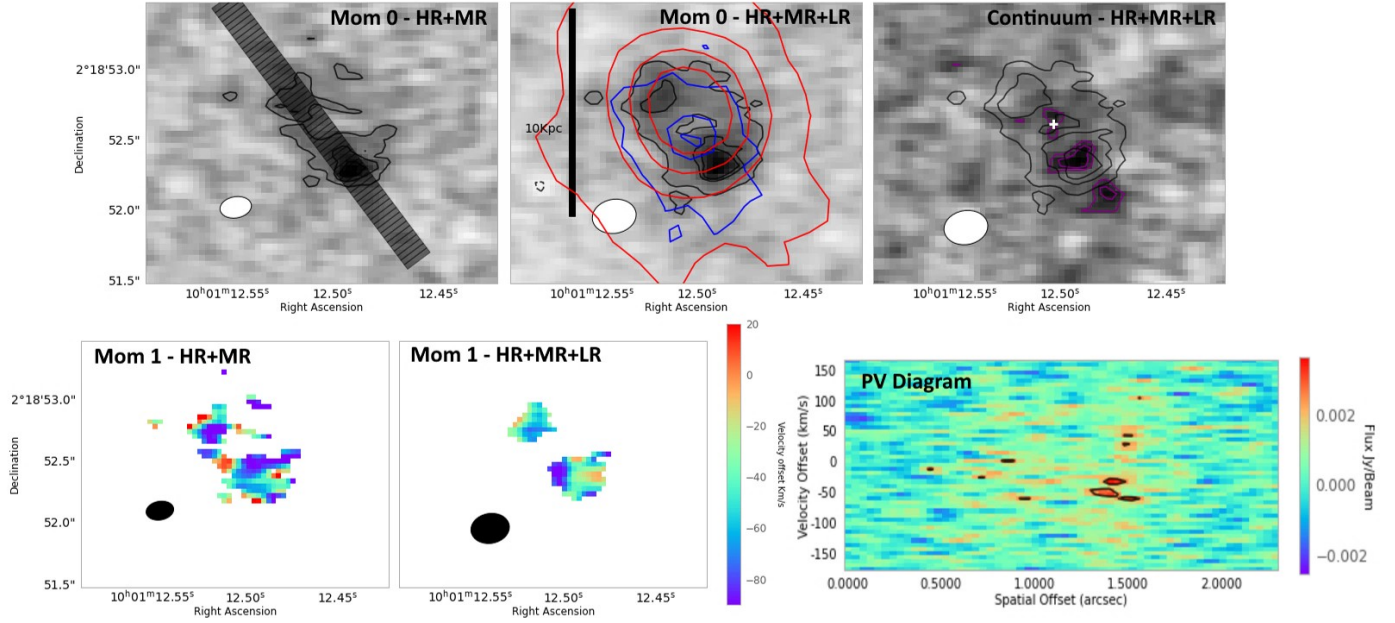


Fig. 2. Summary of maps produced for VC8326. Top line shows the moment 0 maps of VC8326, from left to right: HR+MR (with contours from $\pm 3, 4, 5, \dots \sigma$) and HR+MR+MR – with contours from $\pm 3, 4, 5, \dots \sigma$, along with HST/ACS *F814W* (Koekemoer et al. 2007; blue; 3, 5, 7, 9 σ) and a *K*-band (red; 3, 13, 23, 33 σ) continuum map (with continuum and [CII] contours from 3 σ in purple and black, respectively). The second line shows PV diagram (from the slit shown on the top line taken in the HR+MR concatenation) with contours of 0.7, 0.8, and 0.9 times the peak value) and the moment 1 maps which are cut to 3 and 5 σ , respectively.

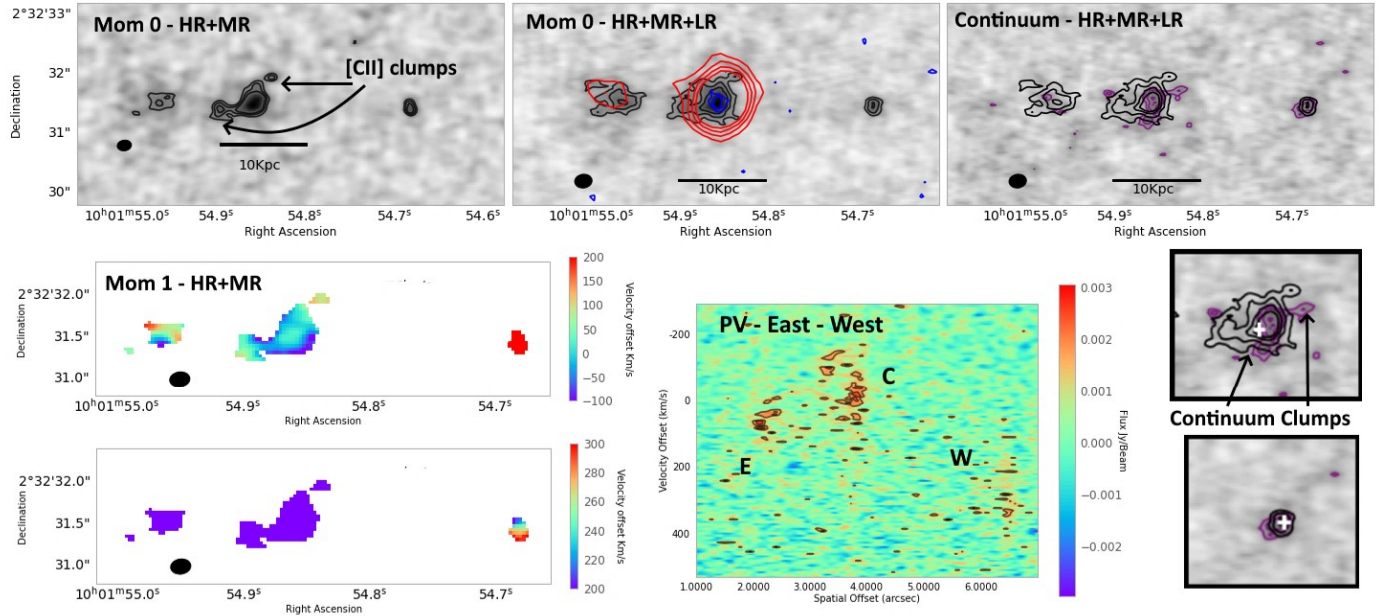


Fig. 3. Summary of maps produced for DC8187. The top row shows the moment 0 maps, from left to right: HR+MR (with contours from $\pm 5, 6, 7, \dots \sigma$) and HR+MR+LR (with contours from $\pm 5, 6, 7, \dots \sigma$), along with HST/ACS *F814W* (Koekemoer et al. 2007; blue; 3, 5, 7, 9 σ) and a *K*-band (red; 3, 4, 5, 6 σ) continuum map (with continuum and [CII] contours from 5 σ in purple and black, respectively). The second line shows the moment 1 maps shown in the HR+MR concatenation and are cut to 5 σ . On the right the second line shows the PV diagram, taken in an east-west slit in the HR+MR concatenation with contours of 0.7, 0.8, and 0.9 times the peak value.

extended faint emission, at the same time, minimising the noise (which increases with aperture size). The noise was estimated with a consistent method to that used in the ALPINE survey (B  thermin et al. 2020) by scaling the error associated to a single beam with the number of synthesised beams per aperture. We note that we did not include flux calibration errors, which can amount to 10% of the total flux.

In the HR+MR+LR concatenation, apertures were selected from diameters smaller than 3'' in diameter for all sources, which this is consistent with the size chosen for the original ALPINE sources in B  thermin et al. (2020). To minimise the effect of noise (which increases with larger aperture sizes), while preventing emission from being missed. The aperture radius is selected by finding the radius where the S/N is maximised. Beyond this

Table 3. Summary of integrated [CII] intensities for each source.

Galaxy	MR+HR flux (Jy km s ⁻¹)	Aperture radius (kpc)	LR+MR+HR flux (Jy km s ⁻¹)	Aperture radius (kpc)	LR ALPINE flux (Jy km s ⁻¹)
DC8737	4.32 ± 0.27	2.5	6.8 ± 0.26	4.5	5.84 ± 0.27
VC8326	2.89 ± 0.36	4.0	3.31 ± 0.29	4.0	2.92 ± 0.23
DC8187(E)	3.05 ± 0.19	2.9	3.54 ± 0.23	4	2.6 ± 0.20
DC8187(C)	4.37 ± 0.19	2.25	5.3 ± 0.23	4.4	4.9 ± 0.30
DC8187(W)	0.74 ± 0.15	1.0	0.95 ± 0.19	1.4	0.8 ± 0.20

point, the additional flux (from an increased aperture) becomes less significant than the increased error (from noise) to minimise the error, whilst ensuring no flux is lost. For the HR+MR concatenation the apertures are generally significantly smaller than the HR+MR+LR concatenation due to fact they trace preferentially the compact emission (and have higher RMS values). We emphasise that when the same aperture is used as in the HR+MR+LR concatenation the HR+MR+LR flux is recovered (within the large errors).

For flux measurements of features within galaxies (clumps or other components), the apertures were manually adjusted, as they are poorly fit by a 2D Gaussian. In these cases, we made sure to ensure that the aperture size was larger than the synthesised beam to ensure an accurate measurement by preventing its flux from being lost.

The integrated fluxes measured for each source are reported in Table 3. For DC8187, photometric measurements were conducted individually for each constituent of the merging system (whilst ensuring no overlap between the apertures). It is clear that the [CII] flux measured for the objects varies significantly across different concatenations, as described in detail in the following.

3.4.1. DC8737

DC8737 is the galaxy with the brightest [CII] Luminosity in the ALPINE survey and shows the largest discrepancy between [CII] fluxes measured in the different configurations. The [CII] emission appears to be dominated by a single component, in all configurations (see the first two lines of Fig. 1).

The total emission in the HR+MR+LR concatenation is 6.80 ± 0.26 Jy km s⁻¹, 60% larger than the flux of the HR+MR concatenation (4.32 ± 0.27 Jy km s⁻¹). This indicates that this object has a significant extended component, indicative of diffuse gas, which is not recovered by the configurations with the highest resolutions. The ALPINE flux is 5.84 ± 0.27 Jy km s⁻¹; whilst this is lower than the flux recovered in this paper, it still supports the presence of an extended gas component.

3.4.2. VC8326

The [CII] emission in VC8326 is resolved into two compact regions when the HR and MR resolution data are included, as can be seen in line 1 of Fig. 2. These compact regions could be interpreted as two merging galaxies (or clumps).

Differently from DC8737, the [CII] fluxes measured for VC8326 in the different configurations all agree within the errors: the fluxes are 2.89 and 3.31 Jy km s⁻¹ for the MR+HR and LR+MR+HR, respectively. The total recovered fluxes in these new concatenations are, within uncertainties, comparable to the original ALPINE flux.

Table 4. Resolved flux measurements of VC8326, all clumps are detected with 100% fidelity.

Source	Flux (HR+MR) (Jy km s ⁻¹)	Aperture diameter (kpc)
Clump SE	0.87 ± 0.15	1.5 × 1.5
Clump NW	0.41 ± 0.13	1.2 × 1.2
Integrated galaxy	3.3 ± 0.48	4 × 4

In addition, we estimated, in the HR+MR+LR concatenation, the amount of [CII] emission that can be associated to the two main components of the objects identified in Fig. 2. We report in Table 4 the apertures that we used and the results of this analysis. We find that the two compact regions make up 26% and 12% of the total [CII] emission of the galaxy VC8326, respectively. Together, therefore, they contain about 38% of the total [CII] flux. The two components are clearly real components as they correspond to a fidelity of 100% (at the 4σ level). As seen in this section and discussed later in the paper, this system is likely a merger; therefore, the remaining emission can be considered a diffuse gas component in this case as well. However, since that in this case the emission is picked up in all concatenations, it is likely less diffuse than in DC8737.

3.4.3. DC8187

DC8187 is constituted of three galaxies at about the same redshift; with the caveat of assuming the observed emission is [CII]. The moment 0 map, shown in Fig. 3, indicates that two of these galaxies (the eastern and central galaxy) are currently interacting, with evidence of two clumps surrounding the central galaxy. The western source (as found in previous papers, see Sect. 2) has no indication of ongoing merging activity and is instead a potential future merger.

The western source is compact. The fluxes are 0.95 and 1.24 Jy km s⁻¹ for the MR+HR and LR+MR+HR concatenations, respectively. Hence, the fluxes are comparable within the error bounds and thus there is no evidence of flux loss between resolutions – indicating that there is no significant extended and diffuse gas component.

The central source presents some flux loss between the HR+MR+LR and HR+MR observations: the fluxes in these two different configurations are 5.3 and 4.37 Jy km s⁻¹, respectively. This suggests that this object is constituted by both a compact and an extended component.

The new observations clearly show that the central source appears to be surrounded by two fainter clumps (as shown in Fig. 3). For this observation, the S/N at which the fidelity reaches 60% is 3.6: the clump in the south-east is detected at 5σ,

Table 5. Resolved flux measurements of DC8187 in HR+MR+LR concatenation, all clumps detected with 100% fidelity.

Source	HR+MR+LR flux (Jy km s ⁻¹)	Aperture diameter (kpc)
Galaxy C	5.3 ± 0.71	8.8 × 8.8
Clump SW	0.68 ± 0.23	2.0 × 2.0
Clump NE	0.30 ± 0.13	1.1 × 1.1

corresponding to a fidelity of 100%; the north-western clump is detected at approximately 4σ – indicating it is a real object. In Table 5, the flux from the clumps is reported. The clumps make up 12 and 5% of the total emission of the central galaxy, respectively; this is a much smaller fraction than for the clumps in VC8326.

The flux loss is less prominent in the eastern source due to the poor detection at the highest resolution and thus large errors associated with it. However, as in the case of the central source, there does appear to be flux loss between the HR+MR and HR+MR+LR concatenations: the fluxes are 3.05 and 3.54 Jy km s⁻¹ for the HR+MR and HR+MR+LR, respectively.

The flux loss in both the central and eastern sources appears to indicate that there is a diffuse gas component. This gas component is likely a consequence of the merger, which is disrupting gas and leading to the formation of gas bridges, extended emission, and clumps – as seen in the moment 0 maps.

3.5. Continuum analysis and radial profiles

As previously mentioned, the 158 μ m continuum is detected in all three systems. In this section, we compare the location and intensity of the FIR emission and that of the [CII], whilst also exploiting [CII] and continuum radial profiles. The radial profiles are obtained integrating the signal ([CII] or continuum) within circular apertures of increasing size (step 1 pixel), starting with a circle that has the same radius as the major axis of the beam. The profiles are centred on the barycentre of the [CII] emission (indicated as a white cross in Figs. 1–3). We note that while for DC8737, this also corresponds to the peak of the [CII] and continuum emission, for VC8326 this barycentre does not correspond to the peak of the [CII] emission (that is concentrated on the two clumps).

We convert the [CII] flux (in Jy km s⁻¹) to a luminosity (in L_{\odot}) using the following equation from Solomon et al. (1992).

$$L_{[\text{CII}]} = 3.25 \times 10^7 S_{\text{CO}} \Delta v \nu_{\text{obs}} D_L^2, \quad (L_{\odot}), \quad (2)$$

where D_L is the luminosity distance in Mpc, $S_{[\text{CO}]} \Delta v$ is the [CII] flux in Jy km s⁻¹, and ν_{obs} is the observed frequency in GHz. As [CII] is often used as a tracer for molecular gas (Zanella et al. 2018), we converted the [CII] luminosity, for each aperture, to the molecular gas mass surface density, using Eq. (3):

$$\Sigma_{\text{gas}} = \alpha_{[\text{CII}]} \frac{1}{D_A^2} L_{[\text{CII}]}, \left(\frac{M_{\odot}}{\text{Mpc}^2} \right), \quad (3)$$

where $\alpha_{[\text{CII}]}$ is the conversion factor between [CII] and molecular gas mass ($31 M_{\odot}/L_{\odot}$, Zanella et al. 2018), $m_{[\text{CII}]}$ is the [CII] Luminosity in L_{\odot} , and D_A is the angular diameter distance in Mpc.

The continuum at 158 μ m is assumed to represent obscured star formation. We converted the continuum flux to surface density of obscured star formation using Eq. (4):

$$\Sigma_{\text{SFR}_{\text{IR}}} = \kappa_{\text{IR}} \frac{1}{D_A^2} \frac{L_{\text{IR}}}{L_{158}} v_{[\text{CII}]} \frac{4\pi D_L^2}{1+z} m_{158}, \left(\frac{M_{\odot}}{\text{Mpc}^2 \text{ yr}} \right), \quad (4)$$

where $L_{[\text{IR}]} / L_{[158]}$ is the ratio between the total infrared luminosity and the 158 μ m rest-frame monochromatic luminosity (we use the value of 1/0.113 as found by Béthermin et al. 2020), $v_{[\text{CII}]}$ is the rest-frame velocity of [CII], $m_{[158]}$ is the flux in Jy of the continuum and $\kappa_{[\text{IR}]}$ is the conversion factor $1.47 \times 10^{-10} M_{\odot}/L_{\odot} \text{ yr}^{-1}$.

The surface density of molecular gas mass and obscured star formation (taken for each aperture) are plotted against the physical of the corresponding aperture. This gives a radial profile of emission of gas and obscured star formation for each Galaxy. These are shown in Fig. 4 and discussed in the next subsections.

3.5.1. DC8737

As discussed in the previous section, DC8737 consists of a compact and an extended [CII] component. From the third panel in the top row of Fig. 1, it is clear that the continuum emission is aligned with the [CII] emission, and is much more compact than the [CII] one. In addition, from the top left panel of Fig. 4, we again see that the obscured SFR, traced by the continuum, is more compact than the molecular gas, traced by [CII].

3.5.2. VC8326

VC8326 consists of two distinct components in [CII], which could be two merging galaxies. However, the continuum shows a radically different morphology: as shown by the right panel of the top row in Fig. 2, the continuum emission is divided into three components, one of which is located at the centre of the galaxy, near the barycentre of the [CII] emission. The other two continuum components (one in the south-western clump and one further south of the galaxy) are both detected at 5σ , corresponding to a fidelity of 100%. It is worth noting, as can be seen in the central panel of the top row in Fig. 2, that this system is also well detected in the *F814W* image by HST and in the *K*-band image by UVISTA (tracing the UV and optical rest-frame, respectively). Both emissions significantly differ from the appearance of the [CII] or continuum emission, as they show only a single component well centred on the barycentre of the [CII] emission, with no evidence of substructure.

From Fig. 4, it is again evident that the [CII] and continuum emission are offset with respect to each other: while the continuum emission monotonically decreases from the centre (chosen as the barycentre of the [CII] emission, shown as a white cross in the top right panel of Fig. 2), the [CII] emission increases for increasingly large apertures until the flux from the two main peaks is included (for the aperture with a 2.5 kpc radius) and then starts decreasing.

This presence of continuum emission in the centre of the system suggests that some amount of obscured star-formation is taking place, although no [CII] emission is detected there. The south-western [CII] component also shows continuum emission, suggestive of a large amount of obscured star formation, which could be feeding from the large gas reservoir traced by [CII].

Finally, there is evidence of a third continuum component with no corresponding [CII] emission (nor HST or VISTA), indicating that there may be an additional component with obscured

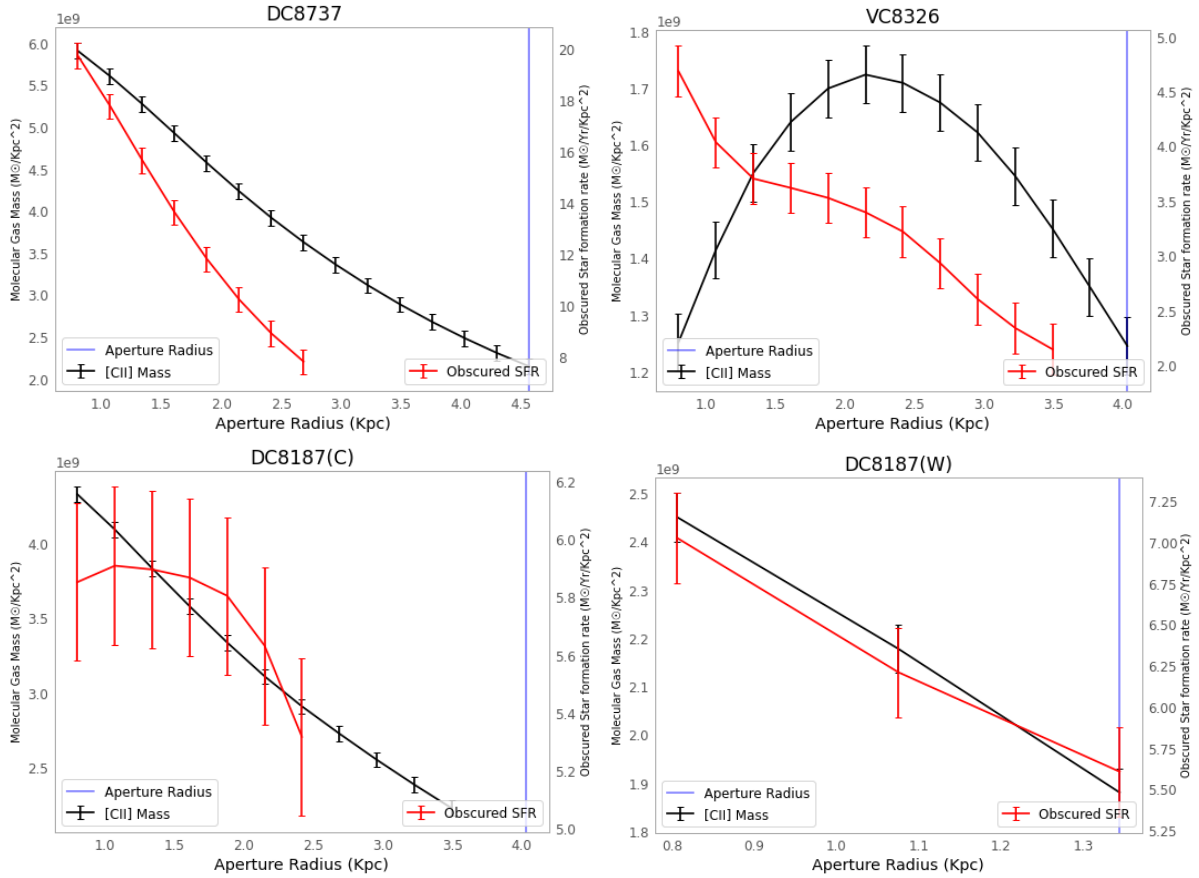


Fig. 4. Radial profiles of the galaxies in this paper with both [CII] and continuum emission (using the HR+MR+LR concatenation). The [CII] emission was converted to a molecular gas surface density and the continuum to an obscured SFR. The aperture of which the galaxies fluxes in Sect. 3.4 were taken in the HR+MR+LR concatenation which is shown by the blue line.

star-formation and with a large quantity of dust (explaining the lack of visible HST emission).

3.5.3. DC8187

As shown by the third panel in the top row of Fig. 3, continuum emission is only significantly detected for the central and western galaxies, while there is no detection in the eastern source. The continuum emission in the central component is coming from three clumps and a central region, as shown in the top row of Fig. 3, and it is concentrated within an area of ~ 3 kpc in diameter, as shown by the radial profile in Fig. 4. At larger radii, the profile drops off – before becoming noise dominated. The clump to the north east is detected at 3σ which is below a 60% fidelity. However the clumps to the south and north-west are detected at 4σ corresponding to 80% fidelity – indicating they are likely to be real. The UV and optical rest-frame emission, traced by HST/ACS *F814W* and *K*-band UVISTA, are very well detected for the central component and aligned with the [CII] emission.

The western galaxy is quite interesting: it is extremely compact at less than ~ 2 kpc in diameter (as it can be seen in Figs. 3 and 4), both in the [CII] and continuum, which have similar profiles.

3.6. Position-velocity diagrams

Position-velocity (PV) diagrams can give important insights on the kinematic properties of galaxies and were therefore produced

for each individual source. PV diagrams are primarily extracted on the HR+MR concatenations or (except for DC8737, where the HR+MR+LR concatenation is used due to the extended nature of the source). The reason for this choice is that this configuration offers the best compromise between resolution and S/N.

PV slits were selected to go through the peak emission for each galaxy – with the slit oriented to, preferentially, go through extended emission or clumps (where detected); a slit width of the average of the minor and major axis of the beam was chosen for all sources. All PV diagrams have contours at fractions of 0.7, 0.8, and 0.9 times of the peak flux in the PV diagram itself. The contours were drawn with this method instead of using the RMS as the RMS is variable within each channel. PV diagrams are shown in the bottom-right panels of Figs. 1–3 and will be analysed in the next sections to constrain the kinematics of these galaxies.

3.7. Spectra

Spectra around the channels containing the [CII] emission were produced for each source (including the individual components of DC8187). Spectra were generated using aperture photometry on each individual channel in the data-cube. The spectra presented in Fig. 4 are extracted in the HR+MR concatenation, with the exception of DC8737, which was obtained from the HR+MR+LR configuration, to cover both the extended and compact components. The HR+MR concatenations of all

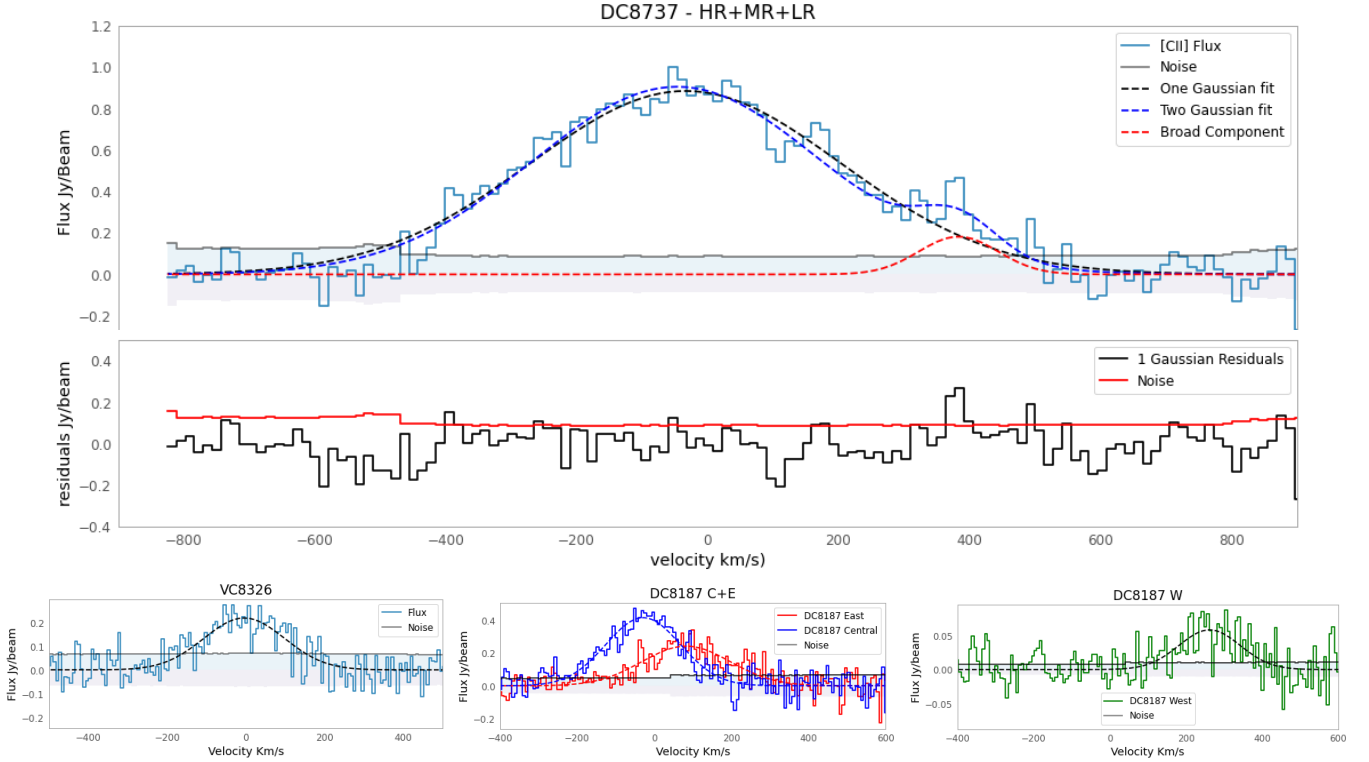


Fig. 5. Spectra of [CII]. Top panel shows the spectrum for DC8737 along with the residuals (middle panel) when the Gaussian fit is subtracted from the data. The bottom three panels show from left to right: the spectra for VC8326, DC8187 (central and east galaxies), and, finally, DC8737 (west galaxy).

sources have a channel width of 6.75 km s^{-1} , the HR+MR+LR of DC8737 has a channel width of 13.5 km s^{-1} . For all sources, the apertures are the same as in Sect. 3.4.

For each source, Gaussian models were fit to the data, including allowing the possibility of multiple Gaussians to fit the data. For all objects but DC8737, one single Gaussian was enough to reproduce the emission. For DC8737, some excess emission around $+400 \text{ km s}^{-1}$ was detected and we therefore added a second Gaussian around that velocity to improve the fit. The middle panel of Fig. 5 shows that the excess emission at $\sim +400 \text{ km s}^{-1}$ is significant at $\sim 3\sigma$.

4. Outflows or mergers in DC8737

Outflows of molecular gas are identified as additional broad emissions, usually offset with respect to the main emission (i.e. [Ginolfi et al. 2020b](#); [Herrera-Camus et al. 2021](#)). The presence of outflows would imply that the total line emission would be best fit by two or three Gaussians, as opposed to a single Gaussian component. As seen in the top panel of Fig. 5, for DC8737 there is evidence of a broad component at $\sim 400 \text{ km s}^{-1}$, in addition to the global emission from the source. In the middle panel of Fig. 5, we show the residual emission when the main Gaussian is subtracted from the total spectrum: the additional emission at $\sim +400 \text{ km s}^{-1}$ is evident as a clear peak that has an integrated S/N of 10.8 (with a peak value of 3σ). We note that there is a second, much smaller peak at $\sim -400 \text{ km s}^{-1}$, with an integrated S/N of 3.6 only. This peak therefore cannot be conclusively distinguished as genuine emission from noise. The fact the two peaks at $\pm 400 \text{ km s}^{-1}$ are of different S/N, and only one is fit by a broad component, is not consistent with the typical scenario of biconical outflow; it would appear that we detect with high significance only the side of the outflow receding from us and not

the approaching side. Although it must be noted that orientation effects are such that even in the case of biconical outflows, only one wing may be observed. The source of this outflow could be the intense star formation identified in the centre of DC8737, we cannot rule out the presence of an active galactic nucleus (AGN), which could also produce such outflows.

We present as well a second scenario, which is consistent with the observed second component at $\sim +400 \text{ km s}^{-1}$: a merging object falling onto the central one at that velocity would be observed an additional emission component, offset with respect to the main one. In Fig. 6, a moment 0 map of only the channels that contribute to the broad component is shown. The map displays a $0.3''$ offset to the south-west compared to the total [CII] emission (comparable to the ALMA beam) further supporting the merger scenario compared to the outflow scenario. However, it is interesting to note that this alleged merging component is not detected neither in the HST/ACS *F814W* image nor in the *K*-band UVISTA one (the only emission in those bands is close to the barycentre of the [CII] emission, see Fig. 1). For the UVISTA, this is expected due to the large PSF ($0.7''$).

By looking at the [CII] moment 0 map for the HR+MR configuration, in the top-left panel of Fig. 1, there is evidence of two smaller additional components: one to the west and the other to the north of the central region. These are well detected at over 4σ , corresponding to a fidelity of 100%, indicating that they are real components. The moment 1 maps, reported in the bottom left panel of the same figure, indicate that these regions both move at an uniform velocity of -200 km s^{-1} with respect to the main component. This suggests that they could be other minor mergers or simply clumps of star formation within the main object. Upcoming JWST data from the COSMOS-Web survey [Casey et al. \(2023\)](#) and with NIRSpec IFU (P.I.: A. Faisst) will allow for this issue to be conclusively determined. These

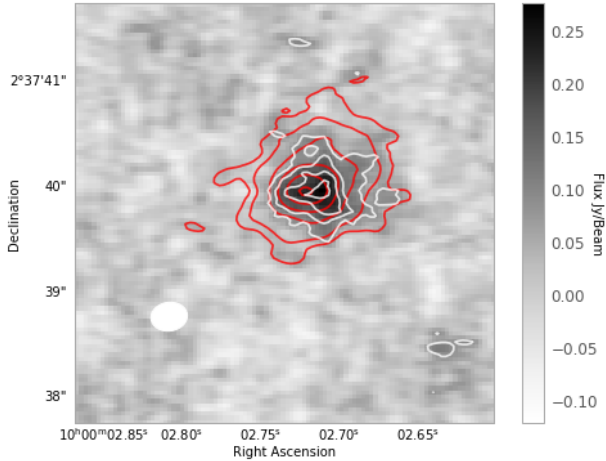


Fig. 6. Map of [CII] for the broad component of DC8737. The contours from $\pm 3, 4, 5, \dots$ are shown in white. The [CII] map created over all line emission is shown by red.

additional components support the hypothesis that DC8737 consists of multiple merging components, thereby explaining its high velocity dispersion. For further details, we refer to the discussion of a similar object [Ginolfi et al. \(2020a\)](#).

5. Discussion

There is only a limited number of high-resolution sub-mm observations of very-high-redshift galaxies ($z > 4$) – targeting molecular gas or continuum emission. The majority of these targets are starbursts which are much brighter and thus easier to detect at a high S/N. Our sample targets the molecular gas and continuum of three MS galaxy systems, which are constituents of five galaxies.

In this section, we summarise all the information that we gathered for the objects in the sample and we discuss the properties of each one individually. We discuss our findings in relation to other observational results and simulations for galaxies observed at the same epoch.

5.1. DC8737

Low-resolution observations (from the original ALPINE survey) of DC8737, the brightest galaxy in the ALPINE survey in [CII], showed no signs of rotation. This suggests the object is an extended dispersion-dominated galaxy. However, the addition of high-resolution observations we present in this work indicate that this object is definitely more complex than initially thought.

In Sect. 3.4, we show that approximately 50% of emission is traced by the HR+MR observations compared to HR+MR+LR. This indicates that there appear to be two components in [CII]: a compact and bright central region and a fainter, more extended component. The higher resolution concatenations only detect the central, compact region, indicating that higher resolutions trace the compact emission as expected; however, these higher resolution concatenations lack the integration time needed to detect the extended components above the noise.

The extended [CII] component is interpreted as a diffuse gas component, similarly to [Fujimoto et al. \(2020\)](#). The compact central region is also detected in HST *F160W* imaging and in the FIR continuum, indicating a highly star forming centre, as presented in [B  thermin et al. \(2023\)](#).

The PV diagram and the HR+MR+LR moment 1 map, shown in Fig. 1, show that the galaxy appears dispersed (with multiple velocities), with no evidence of ordered velocity gradients that could be suggesting rotation. These groups are concentrated in the central, compact region detected in the high-resolution observations. This indicates that the central region could be made up of distinct velocity components. In, the HR+MR map, there is evidence for two components to the north and west of the central region at a velocity of ($< -200 \text{ km s}^{-1}$). This could be indicative of galaxy components (i.e. minor merger), as discussed in Sect. 4.

DC8737 appears to show evidence of an additional [CII] component at $\sim +400 \text{ km s}^{-1}$, which could be interpreted either as outflowing gas or as a minor merger, as discussed in detail in Sect. 4. In support of the outflow scenario, we highlight that the FIR continuum, [CII] and HST maps show intense star formation occurring in the dusty central region, which is expected to drive outflows ([Ginolfi et al. 2020b](#)); although we note the presence of an AGN cannot be excluded for this galaxy. Moreover, the evidence for an extended [CII] halo around the more compact central emission, is in agreement with the recent semi-analytical model by [Pizzati et al. \(2022\)](#), whereby star formation-driven outflows can produce these extended gas halos. In a recent study, [Romano et al. \(2023\)](#) traced outflowing gas in a sample of local dwarf galaxies (analogs of high- z SFGs) from [CII] emission: they found that [CII] is about two times more extended than UV emission, with 40% of the gas possibly pushed outside of the galaxies by the outflow (thus enriching the CGM around those galaxies).

If the additional component were instead due to a minor merger, together with the evidence of fainter, but statistically significant, [CII] components in the moment 0 map (Fig. 1), this could be an indication of a very turbulent environment in which smaller components (or minor mergers) are continuously falling onto the main central galaxy, determining the very large velocity dispersion of the system.

5.2. VC8326

VC8326 is the most complex source in the sample. There is consistency in [CII] flux between the three concatenations for VC8326 – although 62% of the flux is located outside of compact regions (see Sect. 3.4). The fact the [CII] flux from this underlying component is detected in all concatenations suggests that it is less diffuse than the [CII] halo in DC8737. Both concatenations show two clear compact clumps in [CII], which are clearly real emission. For VC8326, the low-resolution observations from ALPINE was unable to resolve the two clumps and the [CII] emission appeared to come from a single component, which was dispersion-dominated; high-resolution data are therefore crucial to reveal the real nature of this system.

Understanding whether VC8326 is composed of two merging galaxies or rather a single galaxy with two in situ clumps is not trivial. The separation of the two [CII] components, around 5 kpc, is much larger than typical galaxies at the same redshift ([Ito et al. 2024](#)), this suggests that they could indeed be two individual merging galaxies. The south-western clump is dusty (seen by emission in the continuum maps in Fig. 2). The size of the clump is consistent with smaller galaxies (i.e. DC8187(W)), which could indicate this is an individual galaxy. There is [CII] located between the two main [CII] components which is comparable to the diffuse [CII] in the rest of the galaxy; the moment 0 map shows an unresolved dip in [CII] that is not real and is, in fact, an effect from the cleaning process. There is strong HST

emission in the centre (and dust continuum emission), which can be explained by merger-induced star formation.

On the other hand, there is some evidence to argue against this scenario. As shown in the middle panel of Fig. 2, rest-frame UV observations from HST indicate intense star formation in the central region, exactly mid-way between the two [CII] compact regions); moreover, this is corroborated by a tentative detection of continuum in the centre (top-right panel of Fig. 2). In addition, there is no HST emission from the clumps and K -band emission tracing the rest-frame optical. Therefore, it is very possible that VC8326 is indeed a large galaxy in formation, with two main clumps of star formation. The brightest is very star-forming and, thus, it has been detected both in [CII] and also in the continuum, while the faintest is not detected in continuum: this could be simply because the latter is less star-forming; therefore, it could be under the ALMA detection limit for the continuum or it could just be younger and therefore less dust-rich.

In any case, we highlight again the presence of a third clump south-west of the [CII] emission that is only detected in continuum (and not in [CII]): this could after-all be an old clump that has exhausted all the gas within it or a less massive dust-rich merging component.

5.3. DC8187

The ALPINE data of this triple system indicated that it was made of three galaxies, but the poor resolution prevented us from analysing their internal properties (Jones et al. 2021). The addition of the high-resolution data in this paper allows us to begin resolving the three sources, leading, for the first time, to the detection of clumps in this system.

In particular, the central galaxy (that is currently interacting with the eastern source) exhibits [CII] clumps surrounding the main component that were not identified with the original ALPINE data (top left panel of Fig. 3). These clumps exhibit a clear separation in velocity from the rest of the galaxy, as shown by the moment 1 map in Fig. 3. These clumps are denser and thus more highly star forming compared to the underlying disk. They are also less bright and less massive than the big clumps seen in VC8326, as they make up only a tiny fraction of the total [CII] emission. This is consistent with simulations (Pallottini et al. 2022), which suggest that mergers may indeed induce clumpy morphologies.

There is also evidence of two clumps detected in the continuum, as shown in the top right panel of Fig. 3 and discussed in Sect. 3.5. These have high fidelity and therefore appear to be real components. It is important to highlight that they are not coincident with the [CII] clumps – this could indicate that clumps with dust obscured star formation are also produced in merging galaxies

Both the central and eastern sources appear to have compact and faint components. This is much more evident in DC8187(C), which appears to have a dusty star-forming, compact centre (detected in the continuum and HST; see Fig. 3) along with a faint diffuse gas component.

The western-most galaxy (which is not strongly interacting with the other two) is compact in [CII] (with an approximate size of $0.3''$ size – 1.1 kpc) when observed in the HR+MR configuration. The velocity map (bottom-left panel of Fig. 3) shows a velocity gradient consistent with rotation. There is no signs of rotation from the PV diagram, likely due to an insufficient S/N, leading to a poor detection in the PV diagram. If this is truly a rotating disk, this presents a case of a low mass disk $z \sim 4.5$.

5.4. Comparison to simulations and literature

So far, the majority of high-resolution [CII] observations at $z > 4.5$ have already been obtained for star-bursting galaxies; therefore, a comparison with our sample of MS galaxies is not straightforward. In particular, Roman-Oliveira et al. (2023) studied a sample of five starbursts and found that four of them are disks, while the remaining galaxy is a merger. All the disks show evidence of non-circular motions (indicative of outflows or minor mergers), different from the smooth rotation seen at lower redshifts. These non-circular motions are consistent with what we have found in our sample, where all galaxies have displayed evidence of mergers or outflows. However we do not see a comparable fraction of disks in our sample (although we note our small sample size).

Herrera-Camus et al. (2021) presented high-resolution [CII] data for a MS galaxy at $z \sim 5.5$. Interestingly, the authors found evidence of outflows and a surrounding gas halo, similarly to what we presented here for our galaxy DC8737, which also shows an extended [CII] halo, a star-forming centre, and evidence of outflows.

Interesting insights can be also derived by comparing our observational results with predictions from simulations. For example, SERRA simulations (Pallottini et al. 2022) predict that the majority of galaxies at $z \sim 6$ have recently undergone a merger. Remarkably, while in the low-resolution ALPINE data, DC8737 and VC8326 were classified as dispersion-dominated galaxies, the high-resolution observations presented in this paper show that these both have signatures of minor mergers, in agreement with the prediction of the SERRA simulations.

We also find an intriguing similarity between some of the features that we presented for DC8187 with the simulated Dahlia galaxy, presented in Pallottini et al. (2017). Simulated observations of Dahlia in [CII] suggested that only 3 out of the 14 satellite clumps identified in the simulation would be detectable with ALMA, with observations similar to the ones presented here; in the case of DC8187, we indeed detected 2 satellite clumps in [CII], consistent with the simulated observations of Dahlia.

The SERRA simulations indicate that mergers can induce clump formation and lead to periods of enhanced star formation, which could be occurring in our identified merging galaxies. The three systems studied in this paper were also the brightest in the ALPINE survey. Whilst [CII] is more tightly correlated with $M(\text{H}_2)$ than with SFR, the increased [CII] flux could be at least partly due to enhanced star formation. However, all our galaxies are MS galaxies, indicating that any mergers are not causing any of our galaxies to be pushed off the MS. In Frias Castillo et al. (2022) a $z = 3.4$ galaxy on the upper end of the MS is studied in CO(1–0). The authors identified that the galaxy is an intermediate merger and, thus, the authors highlighted that mergers can drive physical transformations of galaxies without pushing them off the MS.

It is interesting to highlight that the galaxies we present in this paper turned out to be very diverse; in fact, DC8187(W) is found to be an extremely compact (1.1 kpc) rotating disk. Recent JWST observations (Ferreira et al. 2022) have found that 40% of galaxies at $z \sim 5$ could have disk-like structures, a fraction that is 10 times higher than what was previously found by HST. This suggests that disk formation happens at an earlier epoch and high-redshift galaxies could be much more mature than previously thought. These aforementioned studies with JWST have relied purely on the visual photometric morphologies of such galaxies – and are only tracing star formation in these galaxies.

Our observations of DC8187(W) demonstrate (spectroscopically) that mature disks exist at $z = 4.5$.

6. Conclusions and summary

Using new $0.15''$ resolution ALMA observations in band 7, we have gained new insights into the nature of three primordial MS galaxy systems (one of which is composed of three galaxies) at $z \sim 4.5$, which had previously been studied as part of the ALPINE survey [Le Fèvre et al. \(2020\)](#), [Béthermin et al. \(2020\)](#), [Faisst et al. \(2020\)](#). The new high-resolution data, while it does not reach the sensitivity that was originally requested, have nonetheless revealed many more details than the original ALPINE data. The main conclusions are as follows:

1. VC8326 and DC8737 are the first and third brightest [CII] systems in ALPINE, sharing similar morphokinematic properties in the low-resolution data. However, when observed at high resolution, they turn out to be very different. DC8737 shows a very bright and concentrated [CII] emission in the centre, surrounded by a [CII] halo and a few [CII] fainter clumps. A [CII] component offset by 400 km s^{-1} is also revealed, but we could not conclude whether this indicates an outflow or a merging component. The continuum emission is also aligned with [CII] (although much less extended).
2. VC8326, on the other hand, is resolved by the high-resolution data presented in this paper into two [CII] regions, embedded into an underlying broader component (not as diffuse as the one around DC8737). It is unclear whether these two main [CII] components can be considered two merging galaxies (as suggested by their size and separation) or they are large star-forming regions within the same galaxy (as suggested by the morphology of the UV and optical rest-frame light, revealed by HST and UVISTA, respectively). Moreover, for this object, the continuum emission is also spatially offset with respect to the [CII] emission (except for one of the clumps).
3. DC8187, that is composed of three galaxies, two of which are in the process of interacting with each other, gave us the opportunity to study the effect of mergers on the internal properties of the interacting galaxies. We revealed [CII] and dust bright clumps that were not identified by the low-resolution ALPINE data, which could have been induced by merger activity, as suggested by recent simulations.
4. Remarkably, we also revealed that the third non-interacting galaxy in DC8187 is a compact object that is very likely to be rotating. If confirmed by upcoming JWST NIRSpec-IFU observations, this could be one of the most distant settled disk ever identified.
5. As we increase resolution, the merger fraction increases, indicating we may be underestimating how much mergers contribute to the mass assembly in primordial galaxies.

The addition of these high-resolution observations has interesting implications for our knowledge of galaxy evolution in the first billion year after the Big Bang. The most striking point is that there is evidence of mergers or components in both dispersion-dominated galaxies in this sample. These observations indicate that mergers can be more frequent than what found in the ALPINE survey ([Romano et al. 2021](#)). Whilst our sample remains small, a higher merger fraction would indicate that mergers remain important to the mass assembly of galaxies in this early epoch. It must be noted that the sources identified as potential major mergers (VC8326 and DC8187) are located in

the centre and edge, respectively, of the J1001+0220 protocluster ([Lemaux et al. 2018](#); [Staab et al. 2024](#)). This highlights how environment may be important in shaping galaxy evolution at such redshifts.

We also identify a potential low-mass disk galaxy at redshift $z \sim 4.5$, DC8187(W), in agreement with recent JWST observations: [Ferreira et al. \(2022\)](#) have indicated that disk galaxies might settle much earlier than previously thought, with a larger than expected number of disks in the very early Universe. Furthermore since DC8187(W) is the galaxy with the lowest gas mass in [CII], among those in the triple merger system. This indicates that disks are not necessarily the most mature or massive galaxies at these redshifts.

We also identify clumps in [CII] for a major merging system: DC8187. This supports simulations which show that major mergers can induce clump formation ([Pallottini et al. 2022](#)). In our observations, we observe two distinct categories of clumps: those only visible in [CII] and those only visible in the continuum, but neither of these clumps are visible in HST observations of this galaxy system.

We interpret these clumps as sites of merger-induced star formation: the two categories of clumps are explained by the fact that as time passes, molecular gas is being consumed in the production of stars (and, hence, dust). Therefore, the clumps observed in [CII] might be younger clumps with higher quantities of molecular gas, but still relatively low star-formation activity, whereas the continuum clumps are older clumps where the molecular gas has been fully consumed, but which have larger dust content. The presence of two types of clump indicates star formation may occur over a short period; otherwise, we would only observe one type of clump. The simulations of clumps from [Bournaud et al. \(2014\)](#), [Mandelker et al. \(2014\)](#) indicates that clumps with short bursts of star formation can survive stellar feedback for longer periods ($>500 \text{ Myr}$). This indicates that these clumps could survive timescales long enough for them to migrate to the central component – and be involved the evolution of the galaxy into a settled disk.

Planned JWST observations with NIRSpec/IFU will allow us to perform spatially resolved SED fitting to understand the properties of these clumps and determine if they are comparable to clumps observed at cosmic noon.

Acknowledgements. We would like to thank the anonymous referee for the comments which substantially improved this paper. This paper makes use of the following ALMA data: ADS/JAO.ALMA #2019.1.00226.S. ALMA is a partnership of ESO (representing its member states), NSF (USA) and NINS (Japan), together with NRC (Canada), NSC and ASIAA (Taiwan), and KASI (Republic of Korea), in cooperation with the Republic of Chile. The Joint ALMA Observatory is operated by ESO, AUI/NRAO and NAOJ. E.I. acknowledges funding by ANID FONDECYT Regular 1221846. M.B. gratefully acknowledges support from the ANID BASAL project FB210003 and from the FONDECYT regular grant 1211000. G.E.M. acknowledges the Villum Fonden research grant 13160 “Gas to stars, stars to dust: tracing star formation across cosmic time”, grant 37440, “The Hidden Cosmos”, and the Cosmic Dawn Center of Excellence funded by the Danish National Research Foundation under the grant No. 140. C.H. acknowledges The Flatiron Institute and is supported by the Simons Foundation. M.R. acknowledges support from the Narodowe Centrum Nauki (UMO-2020/38/E/ST9/00077) and support from the Foundation for Polish Science (FNP) under the program START 063.2023. All data is available from telescope archives or upon reasonable request to the authors.

References

- Béthermin, M., Fudamoto, Y., Ginolfi, M., et al. 2020, *A&A*, 643, A2
 Béthermin, M., Accard, C., Guillaume, C., et al. 2023, *A&A*, 680, L8
 Bolatto, A. D., Wolfire, M., & Leroy, A. K. 2013, *ARA&A*, 51, 207
 Bournaud, F., Perret, V., Renaud, F., et al. 2014, *AJ*, 780, 57

- Carilli, C. L., & Walter, F. 2013, *ARA&A*, 51, 105
- Casey, C. M., Kartaltepe, J. S., Drakos, N. E., et al. 2023, *ApJ*, 954, 31
- Cassata, P., Morselli, L., Faisst, A., et al. 2020, *A&A*, 643, A6
- Chabrier, G. 2003, *PASP*, 115, 763
- Claeysens, A., Adamo, A., Richard, J., et al. 2023, *MNRAS*, 520, 2180
- Dekel, A., Sari, R., & Ceverino, D. 2009, *ApJ*, 703, 785
- De Looze, I., Cormier, D., Lebouteiller, V., et al. 2014, *A&A*, 568, A62
- Dessauges-Zavadsky, M., Ginolfi, M., Pozzi, F., et al. 2020, *A&A*, 643, A5
- D'Eugenio, C., Daddi, E., Liu, D., & Gobat, R. 2023, *A&A*, 678, L9
- Di Matteo, P., Bournaud, F., Martig, M., et al. 2008, *A&A*, 492, 31
- Di Teodoro, E. M., & Fraternali, F. 2015, *MNRAS*, 451, 3021
- Faisst, A. L., Schaefer, D., Lemaux, B. C., et al. 2020, *ApJS*, 247, 61
- Ferreira, L., Adams, N., Conselice, C. J., et al. 2022, *ApJ*, 938, L2
- Finkelstein, S. L., Bagley, M. B., Arrabal Haro, P., et al. 2022, *ApJ*, 940, L55
- Förster Schreiber, N. M., & Wuyts, S. 2020, *ARA&A*, 58, 661
- Förster Schreiber, N. M., Genzel, R., Bouché, N., et al. 2009, *ApJ*, 706, 1364
- Frias Castillo, M., Rybak, M., Hodge, J., et al. 2022, *ApJ*, 930, 35
- Fujimoto, S., Silverman, J. D., Bethermin, M., et al. 2020, *ApJ*, 900, 1
- Ginolfi, M., Jones, G. C., Béthermin, M., et al. 2020a, *A&A*, 643, A7
- Ginolfi, M., Jones, G. C., Béthermin, M., et al. 2020b, *A&A*, 633, A90
- Harikane, Y., Ouchi, M., Oguri, M., et al. 2023, *ApJS*, 265, 5
- Herrera-Camus, R., Förster Schreiber, N., Genzel, R., et al. 2021, *A&A*, 649, A31
- Ito, K., Valentino, F., Brammer, G., et al. 2024, *ApJ*, 964, 192
- Jones, G. C., Béthermin, M., Fudamoto, Y., et al. 2020, *MNRAS*, 491, L18
- Jones, G. C., Vergani, D., Romano, M., et al. 2021, *MNRAS*, 507, 3540
- Kennicutt, R. C., Jr. 1998, *ApJ*, 498, 541
- Koekemoer, A. M., Aussel, H., Calzetti, D., et al. 2007, *ApJS*, 172, 196
- Kohandel, M., Pallottini, A., Ferrara, A., et al. 2019, *MNRAS*, 487, 3007
- Le Fèvre, O., Béthermin, M., Faisst, A., et al. 2020, *A&A*, 643, A1
- Lemaux, B. C., Le Fèvre, O., Cucciati, O., et al. 2018, *A&A*, 615, A77
- Litke, K. C., Marrone, D. P., Spilker, J. S., et al. 2019, *ApJ*, 870, 80
- Madau, P., & Dickinson, M. 2014, *ARA&A*, 52, 415
- Maiolino, R., Uebler, H., Perna, M., et al. 2024, *A&A*, in press, <https://doi.org/10.1051/0004-6361/202347087>
- Mandelker, N., Dekel, A., Ceverino, D., et al. 2014, *MNRAS*, 443, 3675
- Naidu, R. P., Oesch, P. A., van Dokkum, P., et al. 2022, *ApJ*, 940, L14
- Neeleman, M., Walter, F., Decarli, R., et al. 2022, *ApJ*, 958, 132
- Oteo, I., Ivison, R. J., Dunne, L., et al. 2018, *ApJ*, 856, 72
- Pallottini, A., Ferrara, A., Bovino, S., et al. 2017, *MNRAS*, 471, 4128
- Pallottini, A., Ferrara, A., Gallerani, S., et al. 2022, *MNRAS*, 513, 5621
- Pizzati, E., Ferrara, A., Pallottini, A., et al. 2022, *MNRAS*, 519, 4608
- Popping, G., Shivaee, I., Sanders, R. L., et al. 2023, *A&A*, 670, A138
- Roman-Oliveira, F., Fraternali, F., & Rizzo, F. 2023, *MNRAS*, 521, 1045
- Romano, M., Cassata, P., Morselli, L., et al. 2021, *A&A*, 653, A111
- Romano, M., Nanni, A., Donevski, D., et al. 2023, *A&A*, 677, A44
- Schreiber, C., Pannella, M., Elbaz, D., et al. 2015, *A&A*, 575, A74
- Shao, Y., Wang, R., Weiss, A., et al. 2022, *A&A*, 668, A121
- Simons, R. C., Kassin, S. A., Snyder, G. F., et al. 2019, *ApJ*, 874, 59
- Solomon, P. M., Downes, D., & Radford, S. J. E. 1992, *ApJ*, 387, L55
- Song, M., Finkelstein, S. L., Ashby, M. L. N., et al. 2016, *ApJ*, 825, 5
- Staab, P., Lemaux, B. C., Forrest, B., et al. 2024, *MNRAS*, 528, 6934
- Tasca, L. A. M., Le Fèvre, O., Hathi, N. P., et al. 2015, *A&A*, 581, A54
- Tomczak, A. R., Quadri, R. F., Tran, K.-V. H., et al. 2016, *ApJ*, 817, 118
- Troncoso, P., Maiolino, R., Sommariva, V., et al. 2014, *A&A*, 563, A58
- Vallini, L., Gallerani, S., Ferrara, A., & Baek, S. 2013, *MNRAS*, 433, 1567
- van der Wel, A., Franx, M., van Dokkum, P. G., et al. 2014, *ApJ*, 788, 28
- Vizgan, D., Greve, T. R., Olsen, K. P., et al. 2022, *ApJ*, 929, 92
- Walter, F., Weiß, A., Downes, D., Decarli, R., & Henkel, C. 2011, *ApJ*, 730, 18
- Walter, F., Decarli, R., Aravena, M., et al. 2016, *ApJ*, 833, 67
- Zanella, A., Daddi, E., Magdis, G., et al. 2018, *MNRAS*, 481, 1976
- Zanella, A., Pallottini, A., Ferrara, A., et al. 2021, *MNRAS*, 500, 118
- Zhang, H., Primack, J. R., Faber, S. M., et al. 2019, *MNRAS*, 484, 5170
-
- ¹ Dipartimento di Fisica e Astronomia, Università di Padova, Vicolo dell'Osservatorio 3, 35122 Padova, Italy
e-mail: Toby.devereaux@studenti.unipd.it
- ² INAF – Osservatorio Astronomico di Padova, Vicolo dell'Osservatorio 5, 35122 Padova, Italy
- ³ Instituto de Física y Astronomía, Universidad de Valparaíso, Avda. Gran Bretaña 1111, Valparaíso, Chile
- ⁴ Université de Strasbourg, CNRS, Observatoire Astronomique 392 de Strasbourg, UMR 7550, 67000 Strasbourg, France
- ⁵ Aix Marseille Université, CNRS, CNES, LAM, Marseille, France
- ⁶ Observatoire de Genève, Université de Genève, 51 Ch. des Maillettes, 1290 Versoix, Switzerland
- ⁷ IPAC, California Institute of Technology, 1200 East California Boulevard, Pasadena, CA 91125, USA
- ⁸ Department of Physics, University of Oxford, Denys Wilkinson Building, Keble Road, Oxford OX1 3RH, UK
- ⁹ INAF – Osservatorio di Astrofisica e Scienza dello Spazio, Via Gobetti 93/3, 40129 Bologna, Italy
- ¹⁰ Instituto de Alta Investigación, Universidad de Tarapacá, Casilla 7D, Arica, Chile
- ¹¹ University of Wisconsin, 475 N Charter Str., Madison, WI, USA
- ¹² University of Massachusetts Amherst, 710 North Pleasant Street, Amherst, MA 01003-9305, USA
- ¹³ Dipartimento di Fisica e Astronomia, Università di Firenze, Via G. Sansone 1, 50019 Sesto Fiorentino, Firenze, Italy
- ¹⁴ INAF – Osservatorio Astrofisico di Arcetri, Largo E. Fermi 5, 50125 Firenze, Italy
- ¹⁵ Instituto de Física, Pontificia Universidad Católica de Valparaíso, Casilla 4059, Valparaíso, Chile
- ¹⁶ Center for Computational Astrophysics, Flatiron Institute, 162 Fifth Avenue, New York, NY 10010, USA
- ¹⁷ Space Telescope Science Institute, 3700 San Martin Dr., Baltimore, MD 21218, USA
- ¹⁸ Department of Physics and Astronomy, University of California Davis, One Shields Avenue, Davis, CA 95616, USA
- ¹⁹ Gemini Observatory, NSF's NOIRLab, 670 N. A'ohoku Place, Hilo, HI 96720, USA
- ²⁰ Cosmic Dawn Center (DAWN), Jagtvej 128, 2200 Copenhagen N, Denmark
- ²¹ DTU-Space, Technical University of Denmark, Elektrovej 327, 2800 Kgs. Lyngby, Denmark
- ²² Niels Bohr Institute, University of Copenhagen, Jagtvej 128, 2200 Copenhagen N, Denmark
- ²³ Departamento de Astronomía, Universidad de La Serena, La Serena, Chile
- ²⁴ Instituto de Investigación Multidisciplinar en Ciencia y Tecnología, Universidad de La Serena, La Serena, Chile
- ²⁵ Instituto de Física y Astronomía, Universidad de Valparaíso, Avda. Gran Bretaña 1111, Valparaíso, Chile
- ²⁶ Dipartimento di Fisica e Astronomia, Università di Bologna, Via Gobetti 93/2, 40129 Bologna, Italy
- ²⁷ National Centre for Nuclear Research, ul. Pasteura 7, 02-093 Warsaw, Poland